

Theoretical characterization of excitation energy transfer in chlorosome light-harvesting antennae from green sulfur bacteria

Takatoshi Fujita,^{1,*} Joonsuk Huh,¹ Semion K. Saikin,¹ Jennifer C. Brookes,^{1,2} and Alán Aspuru-Guzik^{1,†}

¹Department of Chemistry and Chemical Biology, Harvard University, Cambridge, Massachusetts 02138, USA

²Department of Physics and Astronomy, University College London, Gower Street, London WC1E 6BT

Chlorosomes are the largest and most efficient natural light-harvesting antenna systems. They contain thousands of pigment molecules – bacteriochlorophylls (BChls) – that are organized into supramolecular aggregates and form a very efficient network for excitonic energy migration. Here, we present a theoretical study of excitation energy transfer (EET) in the chlorosome based on experimental evidence of the molecular assembly. Our model for the exciton dynamics throughout the antenna combines a stochastic time propagation of the excitonic wave function with molecular dynamics simulations of supramolecular structure, and electronic structure calculations of the excited states. The simulation results reveal a detailed picture of the EET in the chlorosome. Coherent energy transfer is significant only for the first 50 fs after the initial excitation, and the wavelike motion of the exciton is completely damped at 100 fs. Characteristic time constants of incoherent energy transfer, subsequently, vary from 1 ps to several tens of ps. We assign the time scales of the EET to specific physical processes by comparing our results with the data obtained from time-resolved spectroscopy experiments.

I. INTRODUCTION

Chlorosomes of green photosynthetic bacteria are the largest light-harvesting antenna systems found in nature [1–4]. Depending on the bacteria species they consist of bacteriochlorophyll (BChl) *c*, *d*, or *e* molecules that form supramolecular assemblies without protein scaffolding. This finding motivates a strong interest in the design of artificial light-harvesting systems that uses aggregates of pigment or dye molecules [5–9].

In green sulfur bacteria (GSB) – the model system that we study – light energy absorbed by the chlorosome is transferred in the form of Frenkel excitons via a baseplate [10] to an array of Fenna-Matthews-Olson (FMO) complexes [11], which in turn transfers the excitation to reaction centers, where exciton dissociation occurs. Unlike the chlorosome, the baseplate, FMOs, and reaction centers all contain BChls *a* embedded in a protein environment. The impressive energy conversion efficiency of the chlorosome is crucial for the survival of bacteria especially at low light intensities. It has been observed that GSB can live in environments where light intensity can be as low as a few $\mu\text{mol photons m}^{-2} \text{ s}^{-1}$ [12, 13].

The EET in chlorosomes have been studied using various time-resolved spectroscopy techniques [14–23]. For later convenience, we briefly review the excitation energy transfer (EET) time scales measured for chlorosomes from *Chlorobaculum tepidum* (*C. tepidum*), a species of GSB. The chlorosome in this species consists of BChl *c* molecules. One-color transient absorption (TA) measurement in the wavelength region of 750–790 nm has provided four major time constants of 200–300 fs, 1.7–1.8 ps, 5.4–5.9 ps, and 30–40 ps [17]. The authors have assigned the first time to relaxation from higher to lower exciton states, the second and third times to the EET within BChl *c* aggregates in different energy-

transfer steps, and the fourth time component to the EET from BChl *c* aggregates to the baseplate. Qualitatively similar results have been obtained by two-pulse photon echo and one-color TA experiments [18]. A recent two-color TA study with 685 nm pump and 758 nm probe has also yielded four time measurements of 120 fs, 1.1–1.2 ps, 12–14 ps, and 46–52 ps [22], while the authors have regarded all time components as the EET within BChl *c* aggregates. More recently, two-dimensional (2-D) electronic spectra have been measured to explore exciton dynamics during the first 200 fs after excitation [23]. The authors have shown that the amplitude of the positive peak decays with an effective time constant of 40 fs and have explained changes in the 2-D spectra by proposing exciton diffusion on a sub-100 fs time scale. The experiments above have suggested that there are several EET processes in the chlorosomes from sub-100 fs to several tens of ps, while interpretation of them is still controversial.

Electron microscopy (EM) [24–26] supported by theoretical studies [27] have suggested that the BChls are organized into rod-like elements – rolls, while sheet-like aggregates [25, 28] may coexist. This uncertainty in the structural characterization of chlorosomes stems from the large disorder in supramolecular aggregates that compose the chlorosome. Recent understanding of biosynthesis of BChls in *C. tepidum* [29] has led to a well-characterized *bchR*, *bchQ*, and *bchU* three-point mutant [30]. This mutant synthesizes chlorosomes that contain more than 95% BChl *d* and form regularly-packed and tubular-shaped elements [26]. Ganapathy *et al.* [31] have proposed an atomistic structure of the roll from the three-point mutant by using solid-state NMR and cryo-EM images: *Syn-anti* monomer stacks are basic building blocks, and they are organized into coaxial cylinders to form the tubular-shaped elements. Linear dichroism spectra of individual chlorosomes [32] have confirmed that the chlorosomes from the three-point mutant are less disordered than those from the wild type, which is compatible with the highly-symmetric structure proposed by Ganapathy *et al.* [31]. The structure of the roll is illustrated in Figure 1. The *syn-anti* monomer stacks (Figure 1b) run perpendicular to the roll

*Electronic address: tfujita@fas.harvard.edu

†Electronic address: aspuru@chemistry.harvard.edu

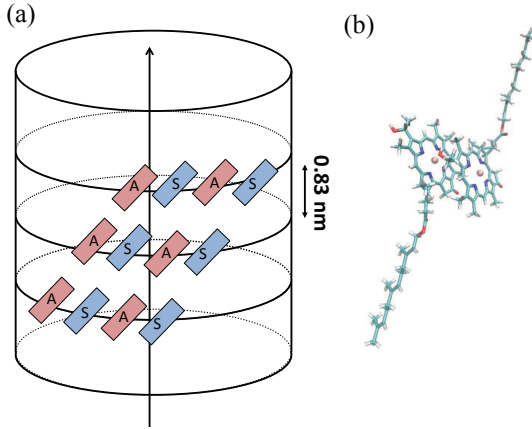


FIG. 1: The structural model of chlorosomes from the three-point mutant [31]. (a) The schematic model of the molecular assembly. (b) The atomistic structure of the *syn-anti* monomer stacks.

symmetry axis; n -BChl pairs form a ring with n -fold rotational symmetry. These rings are stacked in-parallel so that they constitute a helical cylinder (Figure 1a). Several concentric cylinders are further combined with a spacing of the order of 2.1 nm [31].

In our recent letter, [33] we have shown that in the chlorosome based on the structure proposed by Ganapathy *et al.* [31] the memory effects associated with the environment fluctuations – dynamic disorder – assist the exciton diffusion for a broad range of static structural imperfections. In this paper, we present a full report of our work [33] and compare our obtained time scales to those of the experimental results mentioned earlier. The structures of the roll without the baseplate were prepared to model exciton dynamics in the chlorosome. We characterize the EET by combining all-atom molecular dynamics (MD) simulations, time-dependent density functional theory (TDDFT) excited-state calculations, and open quantum system approaches. Our simulations allow for a unified description of the coherent and incoherent energy transfer and depict the overall time evolution of EET processes in the chlorosome.

The remainder of this paper is organized as follows: Section II presents the model of exciton dynamics in the chlorosome. Section III describes details of the site energy and excitonic coupling calculations. Section IV A shows autocorrelation functions and spectral densities from MD/TDDFT calculations. Section IV B presents the optical properties of the roll. The EET in the chlorosome is discussed in Section IV C to F. Section IV G summarizes EET time scales in comparison with the experimental data. We conclude the study by summarizing our results in Section V.

II. THEORY

We first introduce the excitonic Hamiltonian for the chlorosome. Each BChl is treated as a two-level system of ground

and the Q_y excited state, the excitation energy of which depends on the nuclear configuration. In the single exciton approximation, the Hamiltonian for the aggregate of BChls can be written as follows:

$$H = \sum_m \epsilon_m(\mathbf{R}) |m\rangle\langle m| + \sum_{m \neq n} V_{mn}(\mathbf{R}) |m\rangle\langle n| + T(\mathbf{P}) + V_G(\mathbf{R}), \quad (1)$$

where $|m\rangle$ denotes the state where the excitation is localized at m -th BChl (site) and all other sites are in the ground states. $\epsilon_m(\mathbf{R})$ represents an excitation energy of the m -th site in the nuclear configuration \mathbf{R} , and $V_{mn}(\mathbf{R})$ is a excitonic coupling constant between m -th and n -th BChls. Here $T(\mathbf{P})$ and $V_G(\mathbf{R})$ are the kinetic energy and the ground-state potential energy for the nuclear coordinates, respectively. As the next step, we decompose the total Hamiltonian without any assumption of the functional form into a system and bath contributions as:

$$H = H_S + H_{SB} + H_B, \quad (2)$$

$$H_S = \sum_m \langle \epsilon_m \rangle |m\rangle\langle m| + \sum_{m \neq n} V_{mn} |m\rangle\langle n|, \quad (3)$$

$$H_{SB} = \sum_m \Delta\epsilon_m(\mathbf{R}) |m\rangle\langle m|, \quad (4)$$

$$H_B = T(\mathbf{P}) + V_G(\mathbf{R}), \quad (5)$$

where $\Delta\epsilon_m(\mathbf{R}) = \epsilon_m(\mathbf{R}) - \langle \epsilon_m \rangle$. The brackets $\langle \rangle$ denote the average over the nuclear configurations, and the Condon approximation was used in order to omit the dependence of V_{mn} on \mathbf{R} .

The time dependence of the site energies $\epsilon_m(\mathbf{R})$ comes from the dependence of their coordinates \mathbf{R} on time t . This dynamic disorder arising from the nuclear motions is determined by the atomistic simulations. We use MD simulations to generate $\mathbf{R}(t)$ and TDDFT excited-state calculations to obtain $\epsilon(\mathbf{R})$. Thus, in contrast to many studies based on a quantum master equation, this approach can describe the system-bath coupling in complete atomistic detail.

In addition to the dynamic disorder, there is another disorder among excitation energies of the BChls which does not change on the time scales of the exciton dynamics. The physical origins of this static disorder are due to the existence of different homologues of the BChls [30, 34, 35], structural imperfections of supramolecular arrangements, and variations among individual chlorosomes. Experimentally, the disorder among individual chlorosomes is estimated from low temperature spectral hole burning [17, 36] and single molecule fluorescence spectroscopy [32, 37–39]. It is difficult to predict this static disorder from MD simulations. Thus we account for the static disorder by introducing random shifts in the average site energy from a Gaussian distribution $f(\epsilon_m - \langle \epsilon_m \rangle) = 1/\sqrt{2\pi\sigma^2} \exp(-(\epsilon_m - \langle \epsilon_m \rangle)^2/2\sigma^2)$, where σ is the standard deviation for the static disorder. The σ is assumed to be identical for all BChls.

If we treat the nuclear degrees of freedom classically, the wave function of the exciton system is described with the time-dependent Schrödinger equation [40]:

$$i\hbar \frac{\partial}{\partial t} |\psi(t)\rangle = H(t) |\psi(t)\rangle, \quad (6)$$

where $H(t) = H_S + H_{SB}(t)$. In this approach, short MD trajectories are sampled from a full MD trajectory, and the excitonic system is propagated under a unitary evolution for each short MD trajectory. Here it is assumed that the excitonic system does not affect the bath dynamics. The density matrix of the excitonic system ρ is obtained as an average of these unitary evolutions:

$$\rho(t) = \frac{1}{M} \sum_i^M |\psi_i(t)\rangle \langle \psi_i(t)|. \quad (7)$$

A similar approach has been previously applied to small light-harvesting systems such as the FMO complex [41–43] and light-harvesting II complexes of purple bacteria [44, 45].

For a large number of BChls present in the chlorosome, it is computationally unfeasible to calculate site energies of all pigment molecules along an MD trajectory. Here, we take an approximate approach to obtain the site energy fluctuations. Following our previous work on the FMO complex [41], the site energy fluctuations are obtained by solving a set of Langevin equations with white noise:

$$\frac{\partial}{\partial t} \Delta\epsilon_m(t) = -\frac{\Delta\epsilon_m(t)}{\tau_m} + F_m(t), \quad (8)$$

where $F_m(t)$ is a random force; $\langle F_m(t) \rangle = 0$ and $\langle F_m(t)F_m(0) \rangle = 2\langle \Delta\epsilon_m^2 \rangle \delta(t)/\tau_m$. A correlation function from eq 8 is

$$\langle \Delta\epsilon_m(t) \Delta\epsilon_m(0) \rangle = \langle \Delta\epsilon_m^2 \rangle \exp\left(-\frac{t}{\tau_m}\right). \quad (9)$$

This procedure gives the same results as the Kubo-Anderson's stochastic model [46, 47]. The relaxation time of the bath fluctuations, τ_m , can be determined by integrating autocorrelation functions (ACF) of the site energies, $\tau_m = \int_0^\infty dt \langle \Delta\epsilon_m(t) \Delta\epsilon_m(0) \rangle / \langle \Delta\epsilon_m^2 \rangle$. The input parameters to this description of the exciton dynamics are $\langle \Delta\epsilon_m \rangle$, $\langle \Delta\epsilon_m^2 \rangle$, and τ_m , which are obtained from the MD/TDDFT calculations. Owing to the symmetry of the roll, we can assume that the statistical properties of the environmental noise are similar for all the *syn-anti* stacked monomers. Therefore, a random sampling of MD/TDDFT trajectories for a single dimer of *syn* and *anti* BChls can be used for the whole roll.

In order to check the memory effects, we compare our model with the Haken-Strobl-Reineker (HSR) model [48, 49] where the site energy fluctuations do not depend on their memory. In the HSR model, the correlation functions of the site energies are approximated as

$$\langle \Delta\epsilon_m(t) \Delta\epsilon_m(0) \rangle = 2\langle \Delta\epsilon_m^2 \rangle \tau_m \delta(t). \quad (10)$$

Using eq 10, the time evolution of the density matrix can be obtained as follows [48, 49]:

$$\begin{aligned} \frac{\partial}{\partial t} \rho(t) = & -\frac{i}{\hbar} [H_S, \rho(t)] + \sum_m \gamma_m [A_m \rho(t) A_m^\dagger \\ & - \frac{1}{2} A_m A_m^\dagger \rho(t) - \frac{1}{2} \rho(t) A_m A_m^\dagger], \end{aligned} \quad (11)$$

where $A_m = |m\rangle \langle m|$. Here, a pure dephasing rate for the m -th site γ_m is given by [50] $\hbar^2 \gamma_m = 2\langle \Delta\epsilon_m^2 \rangle \tau_m$.

We also construct a classical hopping model using the following equation [51].

$$\frac{\partial}{\partial t} p_m(t) = \sum_n k_{nm} p_n(t) - \sum_n k_{mn} p_m(t), \quad (12)$$

where the hopping rate from m -th to n -th sites k_{mn} is given by [51],

$$k_{mn} = \frac{V_{mn}^2}{\hbar^2} 2\pi \int_{-\infty}^{\infty} d\omega A_m(\omega) F_n(\omega). \quad (13)$$

Here, p_m is a population for m -th site, and $A_m(\omega)$ and $F_n(\omega)$ are normalized absorption and emission and spectra of the m -th and n -th sites, respectively. With the use of eq 10, the absorption and emission lines can be derived as Lorentz functions [51] so that the overlap of the absorption and emission spectra becomes:

$$= \frac{2\pi \int_{-\infty}^{\infty} d\omega A_m(\omega) F_n(\omega)}{\frac{4(\gamma_m + \gamma_n)}{4(\omega_m - \omega_n)^2 + (\gamma_m + \gamma_n)^2}}, \quad (14)$$

where $\hbar\omega_m = \langle \epsilon_m \rangle$.

III. SITE ENERGY AND EXCITONIC COUPLING CALCULATIONS

We set up a model of three-concentric five-stacked (3x5) rings (Figure 2), so that polarizations from several layers can be incorporated into excited-state calculations. Rings from different layers consist of 60, 80 or 100 BChl molecules, and their radii are 6.1, 8.2, and 10.2 nm, respectively. The total number of the BChl molecules in the structure is 1200.

The force field parameters of the BChl d were prepared as follows: One *syn-anti* monomer unit was extracted from Ganapathy's original structure, and the Mulliken charges of the dimer were used as partial charges in the force field. The Mulliken charges were calculated with the Becke three parameter Lee-Yang-Parr hybrid functional [52, 53] and 6-31G** basis set. Other parameters were adopted from the General Amber Force Field [54].

After the geometry optimization, an MD simulation was performed with a time step of 2 fs. The temperature was set at 300 K by the Langevin thermostat. The hydrogen atoms were constrained at their ideal positions using the SHAKE algorithm. After a 1 ns equilibration run, a 20 ps production run

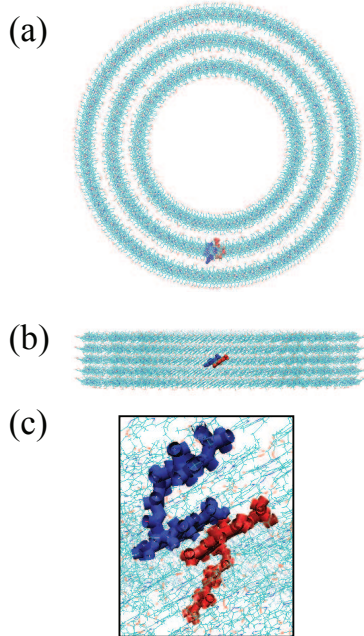


FIG. 2: (a) Top view and (b) side view of a model of three-concentric five-stacked rings for site energy and excitonic coupling calculations. (c) *Syn* (red) and *anti* (blue) monomers in the three-concentric five-stacked rings, the site energies and the TrEsp charges of which were obtained from the excited-state calculations. In (a) and (b), farnesyl tails of the BChls are not shown for clarity.

was carried out and stored every 4 fs. The MD simulation was performed by a CUDA implementation of NAMD [55, 56]. Using the snapshots from the 20 ps trajectory, the Q_y excitation energies for the *syn* and the *anti* monomers (Figure 2c) were obtained. Then, the averages and the two-times correlation functions of the site energies were calculated. TDDFT excited-state calculations were performed with the long-range corrected hybrid functional of Becke [57] and 6-31G basis set in the presence of external point charges of all other molecules, as implemented in the Q-CHEM quantum chemistry package [58]. Results were interpolated to 2 fs time steps.

In our previous paper [33], we employed the point-dipole approximation (PDA) with experimental estimates of the transition dipole moments. This approximation is strictly applicable only if the intermolecular distance is much larger than the size of the molecules [59, 60], which is not the case in the chlorosome where both sizes are comparable. In order to relax the PDA, we decided to apply transition charges from the electrostatic potentials (TrEsp) method [60] as it offers a compromise between accuracy and computational times.

In the TrEsp method [60], the Coulomb interaction between transition densities is approximated as a sum of pairwise interactions of atomic charges. We employ optimally-weighted charges [61] to obtain partial atomic charges from transition densities, where Mulliken charges of the transition

densities were used as the reference. A single pair of *syn-anti* stacked monomers in the 3x5 rings were computed quantum-mechanically (Figure 2c), and all other molecules were treated as external point charges. The transition densities were calculated using multi-layer fragment molecular orbital methods [62] in conjunction with configuration interaction singles and the 6-31G basis set. ABINIT-MP(X) [62, 63] program package was used for the excitonic coupling calculations. Finally, the TrEsp charges of the *syn* and *anti* monomers were used to calculate all excitonic couplings in the structure.

IV. RESULTS AND DISCUSSION

A. Autocorrelation functions and spectral densities

The results of the MD/TDDFT calculations are summarized in Table I. The calculated average site energies are 15243.0 and 15319.4 cm⁻¹ for the *syn* and the *anti* monomers, respectively, and the corresponding standard deviations are 532.2 and 556.5 cm⁻¹. Although the *syn* and the *anti* monomers do not experience the exact same environment, the difference in the averages and standard deviations of the site energy are small. The ACFs and spectral densities for the *syn* and the *anti* monomers are shown in Figure 3. The spectral densities were calculated as a weighted cosine transform of the correlation functions [42, 44, 64]:

$$j_m(\omega) = \frac{\omega}{\pi k_B T} \int_0^\infty dt \langle \Delta\epsilon_m(t) \Delta\epsilon_m(0) \rangle \cos(\omega t). \quad (15)$$

In eq 15 we used a harmonic prefactor in order to negate the temperature dependence of the classical correlation function. [64] In the obtained temperature-independent spectral density, Figure 3b, the strong peaks around 1600 to 2000 cm⁻¹ can be attributed to internal bond stretching in the porphyrin macrocycle of the BChl, while the low-frequency region is ascribed to intermolecular interactions arising from the closed-packed structure.

The reorganization energies 658.7 and 719.9 cm⁻¹ for *syn* and *anti* monomers, respectively, were calculated as $E_R = \int_0^\infty d\omega j(\omega)/\omega$. These values are larger than those calculated from the spectral densities with the standard prefactor [64] in our previous paper [33]. Our MD/TDDFT calculations imply that the reorganization energies of the BChl *d* in the roll is larger than that in solvent (69 cm⁻¹) [65]. This large reorganization energy can be a signature of a fast energy relaxation within Q_y exciton states in the roll.

The chlorosome pigments should be distinguished from ideal J-aggregates where the J-band with the largest oscillator strength is also the lowest exciton state (LES) [17, 36]. Pšenčík *et al.* [17] has shown that LESs in chlorosomes from *C. tepidum* are distributed within 760-800 nm range, while the absorption maximum is at 750 nm. We hypothesise that the relatively large reorganization energy enhances the relaxation from the absorption maximum to the lower exciton states, leading to the energy funneling to the baseplate.

The relaxation time constants for the *syn* and the *anti* monomers were calculated to be 8.80 and 4.51 fs, respectively.

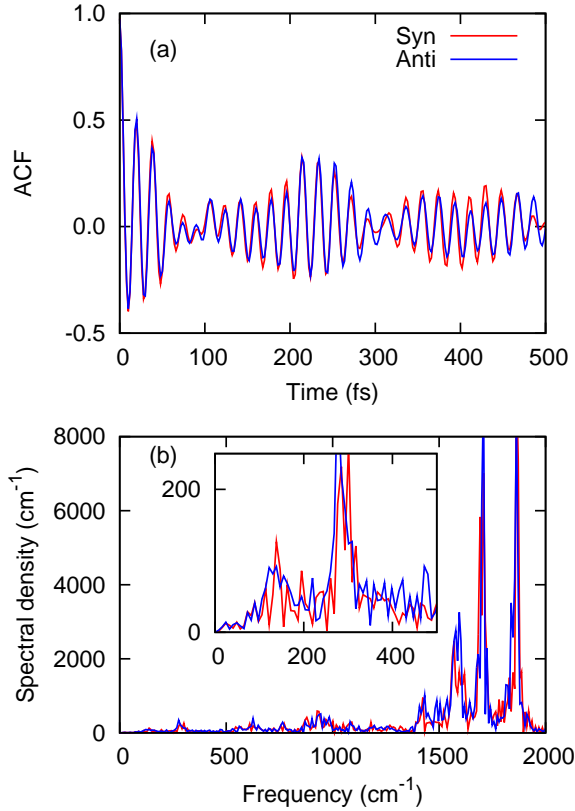


FIG. 3: (a) Autocorrelation functions (ACF) of the site energies and (b) spectral densities for the *syn* (red) and the *anti* (blue) monomers. Low-frequency regions of the spectral densities are shown in the inset.

These values are in good agreement with those estimated by the atomistic simulation for the FMO complex [41, 42]. However, the bath correlation time obtained from fitting to the experimental absorption spectrum of the chlorosome [23] is several times longer than the present values. The reason for this discrepancy can be, for instance, due to the fact that our *ab initio* model assumes a weak electron-vibrational coupling. Moreover, our model accounts for static disorder in the chlorosome, which was not included in the phenomenological model from Ref. 23. We expect that our calculations provide a lower bound estimate for the bath correlations times.

B. Spectra

To compute absorption and circular dichroism (CD) spectra we run simulations of the exciton dynamics using ten-stacked rings (Figure 4a), where each ring is composed of 60 BChls. Initial conditions of the site energy fluctuations $\Delta\epsilon_m(t=0)$ were obtained from the Gaussian distribution with a variance $\langle\Delta\epsilon_m^2\rangle$, and the Euler-Maruyama scheme was applied to solve eq 8 in order to obtain $\Delta\epsilon_m(t)$ and define $H(t)$. Initial conditions of the wave functions were chosen as a localized state on

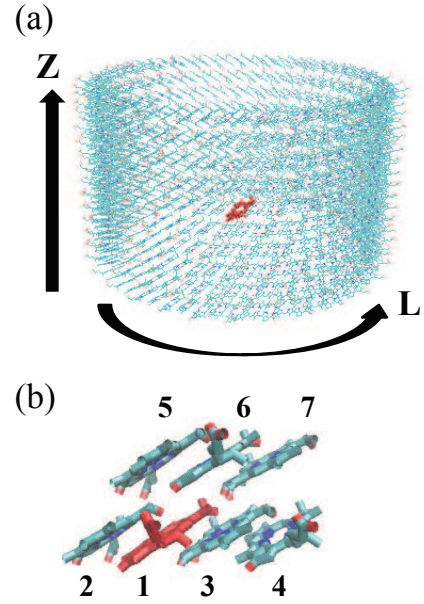


FIG. 4: (a) A model of ten-stacked rings for the exciton dynamics. (b) Initially excited monomer (red) and its neighboring monomers in the ten-stacked rings. In (a) and (b), farnesyl tails of the BChls are not shown for clarity.

an *anti* monomer (Figure 4), and wave functions were propagated with the time step of 1.0 fs by diagonalizing $H(t)$ at each step. The quantum trajectories were averaged over 1000 different realizations of each static disorder.

The absorption and CD spectra were calculated from the exciton propagation by using the following expressions [41, 44]:

$$I_{Abs}(\omega) \propto \text{Re} \int_0^\infty dt e^{i\omega t} \sum_{m,n} \langle \mu_m \cdot \mu_n \rangle \times \{ \langle U_{mn}(t,0) \rangle - \langle U_{nm}^*(t,0) \rangle \}, \quad (16)$$

$$I_{CD}(\omega) \propto \text{Re} \int_0^\infty dt e^{i\omega t} \sum_{m,n} \langle (\mathbf{R}_m - \mathbf{R}_n) \cdot (\mu_m \times \mu_n) \rangle \times \{ \langle U_{mn}(t,0) \rangle - \langle U_{nm}^*(t,0) \rangle \}, \quad (17)$$

where $U_{mn}(t,0)$ is an (m,n) element of the time evolution operator for the $H(t)$.

Treating σ as a phenomenological parameter, we first estimate its value by comparing the calculated spectra with the experiments. Specifically, we compare our result with spectra measured for the wild type of bacteria because optical properties of the three-point mutant are not well established. The full width at half maximum (FWHM) of the absorption spectra

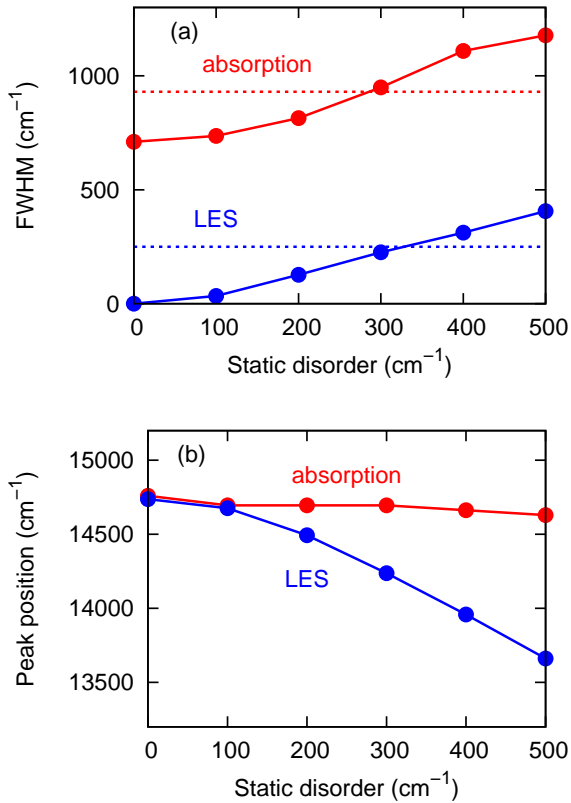


FIG. 5: (a) Full-widths at half maximum (FWHMs) of absorption spectra (red-solid) and the lowest excited state (LES) (blue-solid) as a function of a standard deviation of the static disorder. Experimental linewidths of the absorption spectra (red-dotted) and the LES (blue-dotted) were taken from Refs. 23 and 17, respectively. (b) Peak positions of the absorption spectra (red) and the LES (blue) as a function of a standard deviation of the static disorder.

were calculated as a function of σ and compared with the experimental value from Ref. 23. As both the dynamic and static disorder are included in the exciton dynamics, the linewidth of the absorption spectra computed with eq 16 reflects both homogeneous and inhomogeneous broadening.

In addition to the FWHM of the absorption spectra, we further validate our model by comparing the inhomogeneous broadening of the LES. The inhomogeneous broadening of the LES has been experimentally estimated from the FWHM of the fluorescence spectrum at the temperature of 4 K [17]. To calculate the corresponding linewidth, the LESs were obtained by diagonalizing the system Hamiltonian with the static disorder, and the FWHM were estimated from a standard deviation of 10000 different realizations of the static disorder. The resulting FWHM corresponds to the inhomogeneous broadening of the LES.

Figure 5a shows the FWHMs of absorption spectra and the LES as a function of σ in comparison with the experiments [17, 23]. We found that the both FWHMs can be reproduced with $\sigma = 300$ cm⁻¹.

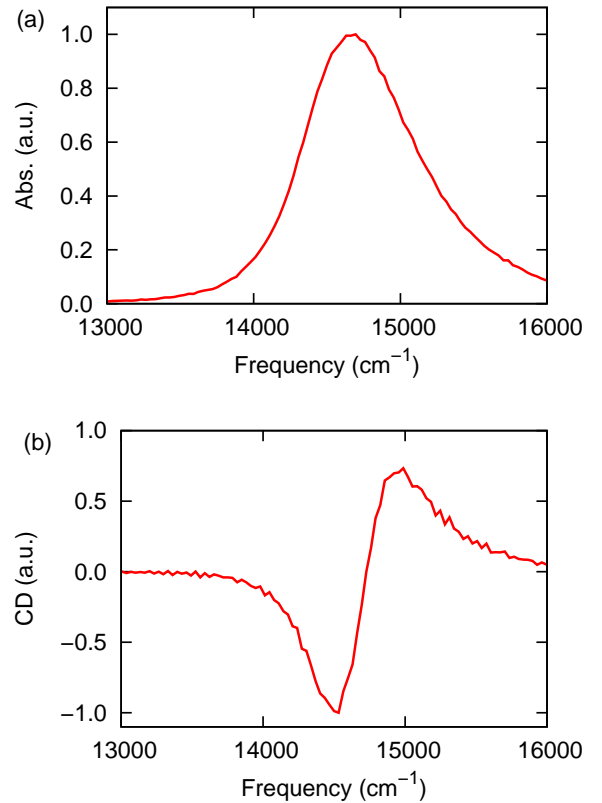


FIG. 6: (a) Absorption and (b) CD spectra obtained from exciton dynamics with the static disorder $\sigma = 300$ cm⁻¹.

The absorption and the CD spectra with $\sigma = 300$ cm⁻¹ are shown in Figure 6. The CD spectrum of chlorosomes from the wild type of *C. tepidum*, for example, has two negative and one positive band [22], whereas there is one positive and one negative peak in another experiment [66]. Our CD spectrum agrees with the one reported by Saga *et al.* [66] and the recently measured spectra for the three-point mutant [67]. Our simulated result further supports the supramolecular structure proposed by Ganapathy *et al.* [31].

Figure 5b shows the peak positions of the absorption maximum and the LES as a function of σ . The peak positions are overestimated compared with the experiments [67]. One of the reasons for that is the small basis set in the TDDFT excited-state calculations. The energy difference between the absorption maximum and the LES is only 23 cm⁻¹ without the static disorder. The absorption maximum is insensitive to σ , while the LES decreases with increasing σ . The energy difference at $\sigma = 300$ cm⁻¹ is 457 cm⁻¹ and in reasonable agreement with about 530 cm⁻¹ estimated for the wild type chlorosome [17].

In the following, we discuss how these results are related to experimental observations. Experimental studies have shown [30, 35] that absorption spectra of chlorosomes from cells grown at low light intensities exhibit red shift up to 100 cm⁻¹. Borrego *et al.* [35] have found that the red shift is

correlated with content of BChl *c* homologues more methylated at C-8² and C-12¹ positions. Chew *et al.* [30] have discussed possible effects of those modifications of BChl *c*. One possibility is that the modifications stabilize formation of larger BChl aggregates which can be assembled into a large chlorosome containing a greater number of BChl *c*. Another possibility is that the modifications increase disorder in the aggregates and allow a much higher packing density of BChl *c* in the chlorosomes without causing crystallizations. Our theoretical calculations show that the peak position of the absorption maximum becomes red-shifted as the static disorder increases. This tendency agrees with the experimental observations. However, the computed shift cannot account for the whole red-shift of the absorption line observed in experiments. Our results are also consistent with the larger linewidths [30] and larger Stokes shifts [35] observed in chlorosomes grown at lower light intensities. It should be noticed that we treat the static disorder with a simplified model of random shifts in the site energies. In contrast, methylation of BChl molecules will have an influence on both site energies and excitonic couplings by distorting the supramolecular arrangements. It remains to be seen how those modifications induce the disorder in the site energies and excitonic couplings at a molecular level.

C. Coherent energy transfer

Here, we will discuss the coherent energy transfer within the roll. In order to show how an exciton is delocalized after the initial excitation of a single site, we compute exciton dynamics using eqs 6, 7, and 8. In addition to the site populations, we present pairwise concurrence between initially excited site and other sites to characterize the role of coherence in the exciton dynamics. The pairwise concurrence [68] is defined as $2 |\langle m | \rho(t) | i \rangle|$, where *i* and *m* refer to the initially excited site and other sites.

Figure 7 shows the population and coherent dynamics of selected monomers calculated with $\sigma = 300 \text{ cm}^{-1}$. The population of initially excited site decays quickly with a time constant of 25 fs without a oscillatory behavior, which reflects large exciton-vibration couplings. The coherences increase and decay within 40-50 fs; these values give an estimate of a decoherence time. The results suggest that the exciton is coherently delocalized within 40-50 fs after the initial excitation of a localized state on a single site, and the coherent propagation is quickly damped due to the dynamic disorder.

In Figures 8 and 9, we show the population and coherence dynamics among the roll at selected times. By comparing Figures 8 and 9, the coherences spread and are suppressed more rapidly than the populations, while transport directions are the same. These features are qualitatively similar for all examined values of the static disorder. The results show that the most of the excitation is distributed over neighboring BChls during the 100 fs after initial excitation, which is comparable to the sub-100 fs exciton diffusion model recently proposed in Ref. 23.

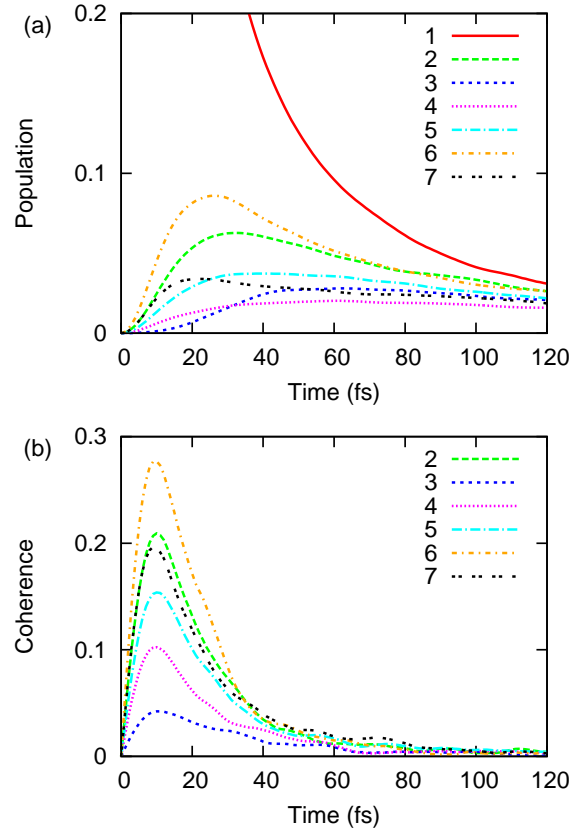


FIG. 7: (a) Populations and (b) coherences of the selected sites neighboring to the initially excited site, which are obtained with the static disorder $\sigma = 300 \text{ cm}^{-1}$. The site numbers refer to corresponding BChls in Figure 4b.

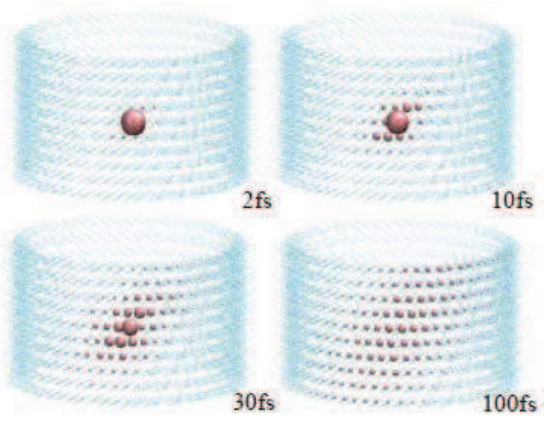


FIG. 8: Populations obtained with the static disorder 300 cm^{-1} at selected times after the initial site excitation. Pink spheres represent Mg atoms of the BChl molecules, and the size of the Mg atom reflects the population value of the BChl molecule.

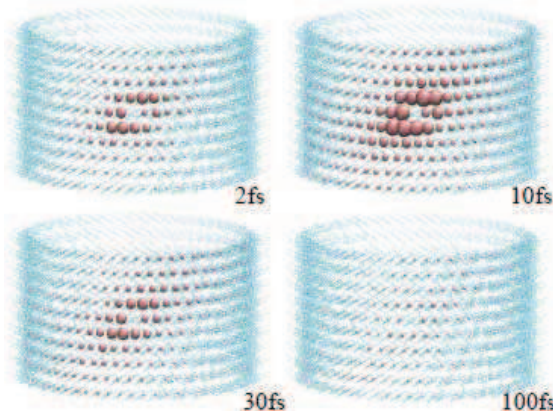


FIG. 9: Coherences obtained with the static disorder $\sigma = 300 \text{ cm}^{-1}$ at selected times after the initial site excitation. Pink spheres represent Mg atoms of the BChl molecules, and the size of the Mg atom reflects the coherent value between the BChl molecule and the initially excited BChl.

D. Exciton diffusion within the roll

To quantify exciton transport on a timescale longer than the decoherence time we compute second moments of the site populations as a function of time. The second moments of the exciton propagation throughout the circumference (M_{LL}) and the coaxial (M_{ZZ}) directions (see Figure 4a) calculated with $\sigma = 300 \text{ cm}^{-1}$ are shown in Figure 10. Both components of the second moment initially scale quadratically and then linearly in time. The transition from the initial ballistic regime to the diffusive regime is observed at 20-30 fs, which is consistent with the time scale of suppression of quantum coherence discussed in the previous section. In contrast to our earlier study with the PDA couplings [33], the results show that M_{LL} is comparable to M_{ZZ} . It has been suggested that the *syn-anti* monomer stacks run perpendicular to the symmetry axis in the chlorosome from three-point mutant [31], while they run parallel to the symmetry axis in the chlorosomes from the wild type of bacteria [31, 69]. Our results may imply that exciton diffusion is insensitive to the supramolecular arrangements, which is relevant to the robust EET.

The second moments calculated using the HSR and hopping model are also shown in Figure 10. The KA model gives the fastest spread of exciton population over the roll, leading to memory-assisted diffusion (MAD). As discussed in Section II, the difference between the KA and the HSR is due to the memory of the bath fluctuations, which is included in the former model. This comparison indicates that the memory of the bath fluctuations enhances the diffusion. The HSR and the hopping models have the same slope with the difference only in the initial ballistic propagation up to around 30 fs.

The mechanism by which the memory effects enhance the diffusion can be explained by considering site-to-site hopping rates. The hopping rate is determined by the overlap between donor fluorescence and acceptor absorption spectra. If

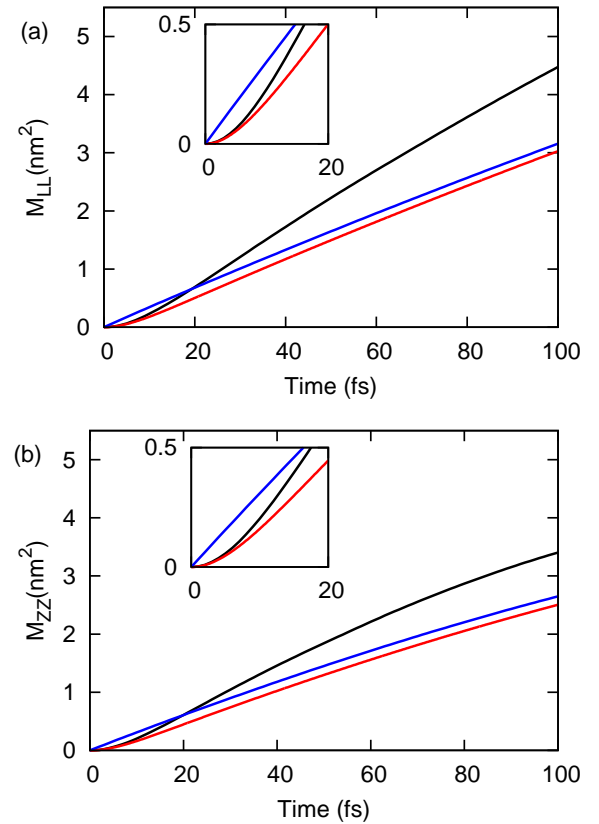


FIG. 10: Second moments of the exciton populations in the (a) circumference (M_{LL}) and (b) coaxial (M_{ZZ}) directions (see Figure 4a) with the static disorder $\sigma = 300 \text{ cm}^{-1}$. Three models compared are Kubo-Anderson (black), Haken-Strobl-Reineker (red), and classical hopping (blue) models.

the correlation function of the site energy is a delta function (HSR model), absorption and fluorescence lineshapes become Lorentzian so that the Franck-Condon factor is an overlap of two Lorentz functions (eq 14). On the other hand, if the correlation function is exponential like the Kubo-Anderson model, lineshapes are closer to the Gaussian [70]. It follows that the KA model gives larger overlap between the donor absorption and the acceptor fluorescence spectra. Therefore, the memory effects of the bath fluctuations give larger hopping rates between pigments and thus lead to the larger exciton diffusion. Note that the memory effects is more pronounced if the bath correlation time is larger than the present value as suggested from the experimental study [23].

Finally, we investigate the dependence of the exciton diffusion on the static disorder. Diffusion coefficients in the circumference and coaxial directions were calculated as a function of σ and are shown in Figure 11. The HSR model gives almost the same diffusion constants as the hopping model: the difference is only in the initial ballistic propagation up to around 30 fs. The KA models gives about twice as large diffusion coefficients as those from the HSR without the static disorder, while the memory effects become small with increasing

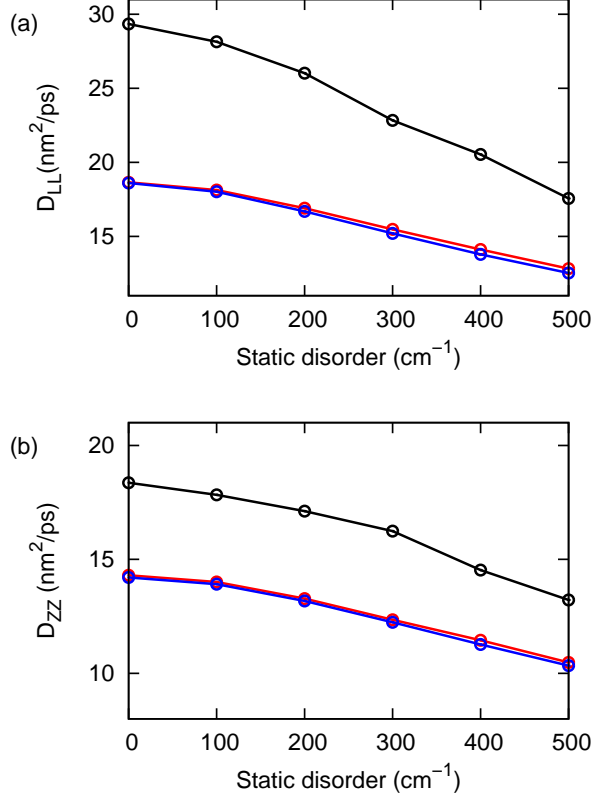


FIG. 11: Exciton diffusion coefficients in the (a) circumference (D_{LL}) and (b) coaxial directions as a function of a standard deviation of the static disorder. Three models compared are Kubo-Anderson (black), Haken-Strobl-Reineker (red), and hopping (blue) models.

σ . The time when an exciton arrives at the opposite site of the roll from the initial site excitation can be used as the time scale of exciton equilibration over the single-layer roll, where the exciton populations are equal for all sites. This time can be calculated as $(R_c\pi)^2/2D_{LL}$, where R_c is the radius of the roll. For the roll of radius $R_c = 6.1$ nm (60 BChl molecules per a ring) with the static disorder of 300 cm $^{-1}$ we obtain the equilibration time to be 8.1 ps.

E. Inter-layer and inter-roll energy transfer

So far we have focused on the single-layer roll, yet chlorosomes may consist of several multi-layer rolls as suggested from EM images [26, 31]. Here we explore the EET among different layers and rolls. We set up two-concentric ten-stacked (2x10) rings and two-roll system consist of 2x10 rings for analysis of the inter-layer and inter-roll EET. Rings from the inner and outer layers consist of 60 and 80 BChls, respectively. Their structures and initial conditions for exciton dynamics are shown in Figure 12b and 13b. In order to speed up our quantum dynamics simulations, we have developed a code for large systems which can propagate wavefunctions in

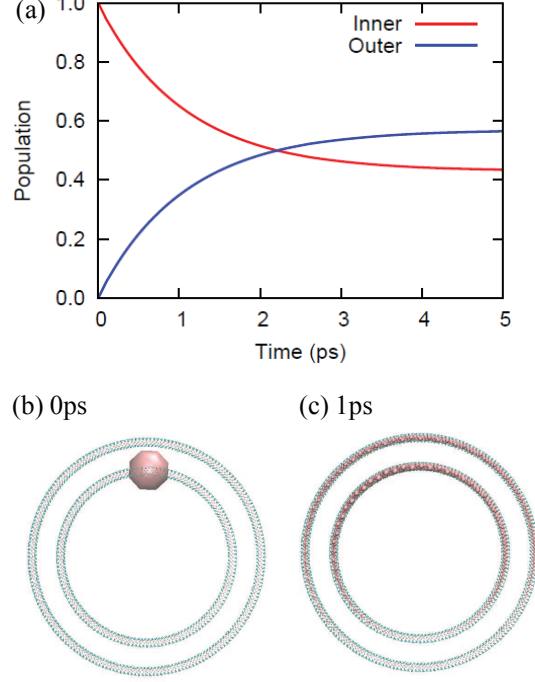


FIG. 12: (a) Exciton populations of the inner (red) and outer layers in two-concentric ten-stacked rings. The structure and exciton populations at (a) 0 and (b) 1 ps are also presented. The pink spheres represent Mg atoms of the BChl molecules, and the size of the Mg atom reflects the population values. In (b) and (c), atoms surrounding the Mg are only shown.

parallel. The simulation conditions are same as those in the earlier sections, and exciton populations were obtained with $\sigma = 300$ cm $^{-1}$.

Figure 12a shows the populations of the inner and outer layers in the 2x10 rings. The single exponential fitting of the inner population yields the time constant of 1.1 ps, and double exponential fitting does not improve the fit. The time of the inter-layer EET is faster than that of the exciton equilibration within the layer. The time scale of exciton equilibration over the outer layer can be estimated as 14.4 ps by taking into account the diameter of the outer layer. The result suggests that for a localized initial excitation the exciton is first distributed among different layers with the characteristic time of 1.1 ps and then equilibrated over the roll in 8.1–14.4 ps, respectively for the inner and outer rolls.

Figure 13a shows the population dynamics between the two double rolls. Exponential fitting for the population of the left roll gives two time constants of 1.4 ps (26%) and 69.8 ps (76%). The faster time component of 1.4 ps is compared to that of inter-layer transfer and thus describes the energy transfer between outer layers of the left and right rolls. Because of the small contact between the rolls, the inter-roll energy transfer becomes slower after the exciton diffuses over the left roll. The inter-roll EET transfer occurs on major time scale of 69.8 ps, which is much larger than the exciton equilibration over

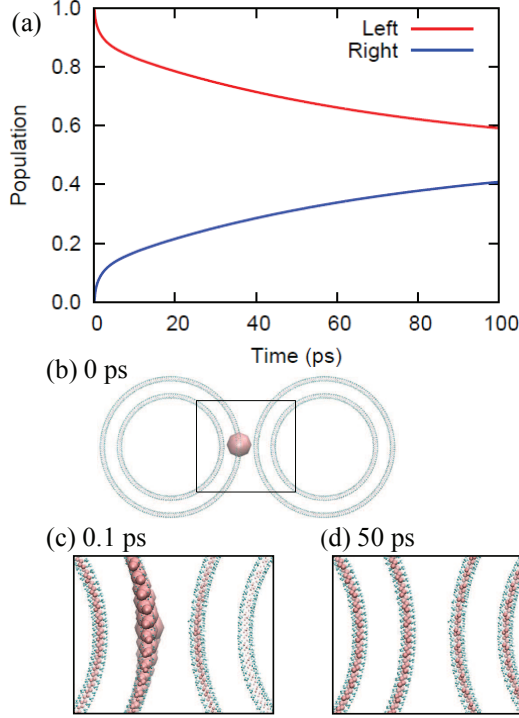


FIG. 13: (a) Exciton populations of the left (red) and right (blue) rolls in the system composed of two two-concentric ten-stacked rings. (b) Top view of the structure and the populations at 0 ps (the initial condition of the exciton dynamics). The exciton populations at (c) 0.1 and (d) 50 ps are also presented. The pink spheres represent Mg atoms of the BChl molecules, and the size of the Mg atom reflects the population values. In (b)-(d), atoms surrounding the Mg are only shown.

the single roll. Note that the two-roll system is an extreme structure. In chlorosomes, a roll may be surrounded by other rolls or lamellar layers [26]. Thus, the estimated time constants 1.4 and 69.8 ps can be considered as the lower and the upper bounds of the inter-layer energy transfer time scale.

F. Anisotropy decay

Fluorescence anisotropy decay has been used in the analysis of the lifetimes of coherent energy transfer. [71–77] Following Ref. 77, we calculate the fluorescence anisotropy decay based on the exciton dynamics. In the exciton propagation model we have added the ground state and the off-diagonal system-radiation Hamiltonian, $H_{ij}(t) = \mathbf{E}(t) \cdot \mu_{ij}$ to eq 3. Here $\mathbf{E}(t)$ is an electric field for a stimulating pulse, and μ_{mn} is a dipole moment operator. An (i,j) component of polarization tensor α_{ij} is defined as the i -th component of the dipole moment after applying an electric field polarized in the j direction. The anisotropy decay $r(t)$ can be calculated as $r(t) = 3\gamma^2/(45\alpha^2 + 4\gamma^2)$, where α and γ are isotropic and anisotropic tensor invariants of polarization tensor, respectively [78]. An initial condition was chosen as the ground

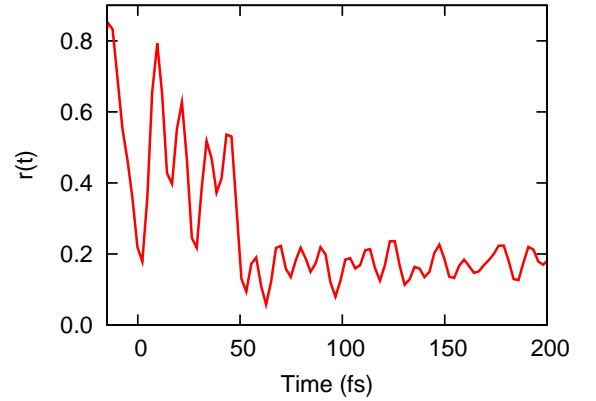


FIG. 14: The polarization anisotropy decay of the three-staked rings with the static disorder $\sigma = 300 \text{ cm}^{-1}$.

state $\rho = |G\rangle\langle G|$, and an 8 fs Gaussian-enveloped electric field of frequency 14890 cm^{-1} was applied as the stimulating pulse. We use the three-stacked rings to calculate the anisotropy decay.

Figure 12 shows the polarization anisotropy decay for the three-stacked rings structure. The initial value of the anisotropy is close to 0.8, and the residual value is about 0.18. The anisotropy shows the oscillatory behavior within 50 fs after the stimulating pulse, reflecting wavelike motion of the exciton. Single exponential fitting to the anisotropy profile yields 30 fs as the depolarization time. The depolarization time can be compared to the decoherence time estimated from the coherences in site basis in Section IV C. Note that the ultrafast depolarization time of sub-100 fs has not been resolved by earlier time-dependent polarization anisotropy experiments [15, 16, 20, 22]. For example, the one-color TA anisotropy in the wavelength region of 720-790 nm has given a single decay time of 1.7-3.9 ps [16]. However, the ultrafast decay of the anisotropy has been observed by a recent pump-probe measurement of the chlorosome from *Chlorobium Phaeobacterioides* (Jeongho Kim personal communication), which is consistent with the present result.

G. Time scales

In this final section, we summarize the various time scales of EET obtained from our simulations. Table II shows the theoretical time scales in comparison with experimental time scales measured for chlorosomes from wild type of *C. tepidum*. It should be noticed that the EET time scales may be affected by the presence of the baseplate acting as an exciton drain, which lies outside the scope of this paper. Exciton dynamics in the whole light-harvesting system, which is composed of the chlorosome, baseplate, and FMO complexes, is being studied in our group, which will be submitted elsewhere.

The experimental studies [17, 18, 22] have suggested that there are four major time constants in the EET processes.

Here, we compare our results with the time components of 120 fs, 1.1-1.2 ps, 12-14 ps, and 46-52 ps which were obtained with 685 nm pump and 758 nm probe [22], which should have a minimal contribution from the baseplate BChl *a*. Our simulations show the coherent propagation of excitons for the initial 50 fs after excitation. The lifetime of this coherent energy transfer can be estimated from the decoherence time and the depolarization time. The first component of 120 fs can be associated with the coherent EET which describes wavelike motions of the exciton. The depolarization times of 30 fs is smaller than the first component of the TA experiments. A possible reason for this is that in terms of the Bloch equation interpretation, the time components of the TA experiments will describe the population decay (T_1) time, while the depolarization time includes a pure dephasing time (T_2') as well [71, 73]. The incoherent EET subsequently takes places after the ultrafast process. We have obtained 1.1 ps for the inter-layer EET within a single roll and 1.4 ps for the energy transfer between neighboring layers of the double rolls. The time scale of 1.1-1.4 ps is in good agreement with the second time component of 1.1-1.2 ps; the second component describes the inter-layer energy transfer. The 8.1-14.1 ps time is comparable to the third component of 12-14 ps, suggesting that the third component reflects the exciton equilibration within single roll. The time constant of 69.8 ps corresponds qualitatively to the 46-52 ps. The forth time component is tentatively assigned as the exciton equilibration over different rolls, while this would not be the case if a roll were surrounded by lamellar layers.

Based on the interpretations above, we speculate on the corresponding time scales of the EET in the chlorosomes based on the structure from the three-point mutant. The first component describes the lifetime of the coherent energy transfer which largely depends on the exciton-vibration coupling. Reorganization energies will be similar for the wild type and the three-point mutant as long as the local packing structure is same. Therefore, the first component reflecting the coherent energy transfer may be similar for the wild type and the three-point mutant. We also expect that the second component describing the inter-layer EET is similar for the wild type and the three-point mutant, because the same 2.1 nm spacing was observed for both the wild type and the three-point mutant [26, 31]. The third component describing the energy equilibration over the roll is sensitive to a radius of the roll. The EM study [26] finds that the diameter of the roll of the three-

point mutant is larger than that of the wild type. According to our interpretation and the experimental observation, the third time component of the three-point mutant will be larger than that of the wild type. This could be an experimental verification of our assignment of the experimental time scales.

V. CONCLUSIONS

In this work, we have characterized the EET in the chlorosome by combining MD simulations, excited-state calculations with TDDFT, and stochastic propagation of excitonic wave function. Our study shows that the coherent energy transfer occurs for 50 fs after the initial excitation, and the wavelike motion of the exciton is damped to vanish in 100 fs due to the dynamic disorder. The incoherent energy transfer subsequently takes place in the characteristic time constants from 1 ps to several tens of ps. The existence of multiple time scales reflects a hierarchy of the structures in the chlorosomes. We have interpreted the experimental time scales in terms of the theoretical results and also presented a possible verification of our assignment.

ACKNOWLEDGMENT

The authors would like to thank Prof. Huub J. M. de Groot for fruitful discussions and the donation of the *syn-anti* chlorosome configuration template. We further appreciate Stéphanie Valneau and Prof. Jeongho Kim for very useful discussions. T.F. thanks John Parkhill for advice on the calculations of the anisotropy decay and Yoshio Okiyama for providing a module of the optimally-weighted charge. T. F., J. H., and A. A.-G. acknowledge support from the Center for Excitonics, an Energy Frontier Research Center funded by the US Department of Energy, Office of Science and Office of Basic Energy Sciences under award DE-SC0001088. J. C. B. acknowledges support from Wellcome Trust UK. S. K. S. and A. A.-G. also acknowledge Defense Threat Reduction Agency grant HDTRA1-10-1-0046. Further, A. A.-G. is grateful for the support from Defense Advanced Research Projects Agency grant N66001-10-1-4063, Camille and Henry Dreyfus Foundation, and Alfred P. Sloan Foundation

[1] Olson, J. M. *Photochem. Photobiol.* **1998**, *67*, 61–75.

[2] Blankenship, R. E.; Olson, J. M.; Miller, M. In *Anoxygenic Photosynthetic Bacteria*; Blankenship, R. E., Madigan, M., Bauer, C. E., Eds.; Springer Netherlands, 2004; pp 399–435.

[3] Oostergetel, G. T.; van Amerongen, H.; Boekema, E. J. *Photosynth. Res.* **2010**, *104*, 245–255.

[4] Hohmann-Marriott, M. F.; Blankenship, R. E. *Annu. Rev. Plant Biol.* **2011**, *62*, 515–548.

[5] Prokhorenko, V. I.; Holzwarth, A. R.; Müller, M. G.; Schaffner, K.; Miyatake, T.; Tamiaki, H. *J. Phys. Chem. B* **2002**, *106*, 5761–5768.

[6] Balaban, T. S. *Acc. Chem. Res.* **2005**, *38*, 612–623.

[7] Röger, C.; Miloslavina, Y.; Brunner, D.; Holzwarth, A. R.; Würthner, F. *J. Am. Chem. Soc.* **2008**, *130*, 5929–5939.

[8] Miyatake, T.; Tamiaki, H. *Coord. Chem. Rev.* **2010**, *254*, 2593–2602.

[9] Eisele, D. M.; Cone, C. W.; Bloemsma, E. A.; Vlaming, S. M.; van der Kwaak, C. G. F.; Silbey, R. J.; Bawendi, M. G.; Knoester, J.; Rabe, J. P.; Bout, D. A. V. *Nat. Chem.* **2012**, *4*, 655–662.

[10] Pedersen, M. O.; Linnanto, J.; Frigaard, N.-U.; Nielsen, N. C.; Miller, M. *Photosynth. Res.* **2010**, *104*, 233–243.

[11] Olson, J. *Photosynth. Res.* **2004**, *80*, 181–187.

[12] Overmann, J.; Cypionka, H.; Pfennig, N. *Limnol. Oceanogr.* **1992**, *37*, 150–155.

[13] Beatty, J. T.; Overmann, J.; Lince, M. T.; Manske, A. K.; Lang, A. S.; Blankenship, R. E.; Dover, C. L. V.; Martinsson, T. A.; Plumley, F. G. *Proc. Natl. Acad. Sci. U.S.A.* **2005**, *102*, 9306–9310.

[14] Causgrove, T.; Brune, D.; Wang, J.; Wittmershaus, B.; Blankenship, R. *Photosynth. Res.* **1990**, *26*, 39–48.

[15] Savikhin, S.; Zhu, Y.; Lin, S.; Blankenship, R. E.; Struve, W. S. *J. Phys. Chem.* **1994**, *98*, 10322–10334.

[16] Savikhin, S.; van Noort, P. I.; Zhu, Y.; Lin, S.; Blankenship, R. E.; Struve, W. S. *Chem. Phys.* **1995**, *194*, 245–258.

[17] Pšenčík, J.; Polívka, T.; Němec, P.; Dian, J.; Kudrna, J.; Malý, P.; Hála, J. *J. Phys. Chem. A* **1998**, *102*, 4392–4398.

[18] Prokhortenko, V. I.; D. B. Steensgaard, D. B.; Holzwarth, A. R. *Biophys. J.* **2000**, *79*, 2105–2120.

[19] Pšenčík, J.; Ma, Y.-Z.; Arellano, J.; Garcia-Gil, J.; Holzwarth, A.; Gillbro, T. *Photosynth. Res.* **2002**, *71*, 5–18.

[20] Pšenčík, J.; Ma, Y.-Z.; Arellano, J. B.; Halá, J.; Gillbro, T. *Biophys. J.* **2003**, *84*, 1161–1179.

[21] Martiskainen, J.; Linnanto, J.; Kananavicius, R.; Lehtovuori, V.; Korppi-Tommola, J. *Chem. Phys. Lett.* **2009**, *477*, 216–220.

[22] Martiskainen, J.; Linnanto, J.; Aumanen, V.; Myllyperkiö, P.; Korppi-Tommola, J. *Photochem. Photobiol.* **2012**, *88*, 675–683.

[23] Dostál, J.; Mančal, T.; Augulis, R.-n.; Vácha, F.; Pšenčík, J.; Zigmantas, D. *J. Am. Chem. Soc.* **2012**, *134*, 11611–11617.

[24] Staehelin, L. A.; Golecki, J. R.; Fuller, R. C.; Drews, G. *Arch. Microbiol.* **1978**, *119*, 269–277.

[25] Hohmann-Mariott, M.; Blankenship, R.; Roberson, R. *Photosynth. Res.* **2005**, *86*, 145–154.

[26] Oostergetel, G. T.; Reus, M.; Chew, A. G. M.; Bryant, D. A.; Boekema, E. J.; Holzwarth, A. R. *FEBS Lett.* **2007**, *581*, 5435–5439.

[27] Linnanto, J.; Korppi-Tommola, J. *Photosynth. Res.* **2008**, *96*, 227–245.

[28] Pšenčík, J.; Ikonen, T. P.; Laurinmäki, P.; Merckel, M. C.; Butcher, S. J.; Serimaa, R. E.; Tuma, R. *Biophys. J.* **2004**, *87*, 1165–1172.

[29] Gomez Maqueo Chew, A.; Bryant, D. A. *Annu. Rev. Microbiol.* **2007**, *61*, 113–129.

[30] Gomez Maqueo Chew, A.; Frigaard, N. U.; Bryant, D. A. *J. Bacteriol.* **2007**, *189*, 6176–6184.

[31] Ganapathy, S.; Oostergetel, G. T.; Wawrzyniak, P. K.; Reus, M.; Gomez Maqueo Chew, A.; Buda, F.; Boekema, E. J.; Bryant, D. A.; Holzwarth, A. R.; de Groot, H. J. M. *Proc. Natl. Acad. Sci. U.S.A.* **2009**, *106*, 8525–8530.

[32] Furumaki, S.; Vacha, F.; Habuchi, S.; Tsukatani, Y.; Bryant, D. A.; Vacha, M. *J. Am. Chem. Soc.* **2011**, *133*, 6703–6710.

[33] Fujita, T.; Brookes, J. C.; Saikin, S. K.; Aspuru-Guzik, A. *J. Phys. Chem. Lett.* **2012**, *3*, 2357–2361.

[34] Huster, M. S.; Smith, K. M. *Biochemistry* **1990**, *29*, 4348–4355.

[35] Borrego, C.; Gerola, P.; Miller, M.; Cox, R. *Photosynth. Res.* **1999**, *59*, 159–166.

[36] Fetisova, Z. G.; Mauring, K.; Taisova, A. S. *Photosyn. Res.* **1994**, *41*, 205–210.

[37] Saga, Y.; Wazawa, T.; Mizoguchi, T.; Ishii, Y.; Yanagida, T.; Tamiaki, H. *Photochem. Photobiol.* **2002**, *75*, 433–436.

[38] Shibata, Y.; Saga, Y.; Tamiaki, H.; Itoh, S. *Biophys. J.* **2006**, *91*, 3787–3796.

[39] Tian, Y.; Camacho, R.; Thomsson, D.; Reus, M.; Holzwarth, A. R.; Scheblykin, I. G. *J. Am. Chem. Soc.* **2011**, *133*, 17192–17199.

[40] May, V.; Kühn, O. *Charge and Energy Transfer Dynamics in Molecular Systems*, 3rd ed.; Wiley-VCH: Berlin, 2011.

[41] Shim, S.; Rebentrost, P.; Valleau, S.; Aspuru-Guzik, A. *Biophys. J.* **2012**, *102*, 649–660.

[42] Olbrich, C.; Strümpfer, J.; Schulten, K.; Kleinekathöfer, U. *J. Phys. Chem. Lett.* **2011**, *2*, 1771–1776.

[43] Olbrich, C.; Jansen, T. H. C.; Liebers, J.; Aghtar, M.; Strümpfer, J.; Schulten, K.; Knoester, J.; Kleinekathöfer, U. *J. Phys. Chem. B* **2011**, *115*, 8609–8621.

[44] Damjanović, A.; Kosztin, I.; Kleinekathöfer, U.; Schulten, K. *Phys. Rev. E* **2002**, *65*, 031919.

[45] Olbrich, C.; Kleinekathöfer, U. *J. Phys. Chem. B* **2010**, *114*, 12427–12437.

[46] Anderson, P. W. *J. Phys. Soc. Jpn.* **1954**, *9*, 316–339.

[47] Kubo, R. *J. Phys. Soc. Jpn.* **1954**, *9*, 935–944.

[48] Haken, H.; Reineker, P. *Z. Phys.* **1973**, *249*, 253–268.

[49] Haken, H.; Strobl, G. *Z. Phys.* **1973**, *262*, 135–148.

[50] Breuer, H.-P.; Petruccione, F. *The Theory of Open Quantum Systems*; Oxford University Press: New York, 2002.

[51] Ern, V.; Suna, A.; Tomkiewicz, Y.; Avakian, P.; Groff, R. P. *Phys. Rev. B* **1972**, *5*, 3222–3234.

[52] Becke, A. D. *J. Chem. Phys.* **1993**, *98*, 5648–5652.

[53] Lee, C. T.; Yang, W. T.; Parr, R. G. *Phys. Rev. B* **1988**, *37*, 785–789.

[54] Wang, J.; Wolf, R. M.; Case, D. A.; Kollman, P. A. *J. Comput. Chem.* **2004**, *25*, 1157–1174.

[55] Phillips, J. C.; Braun, R.; Wang, W.; Gumbart, J.; Tajkhorshid, E.; Villa, E.; Chipot, C.; Skeel, R. D.; Kalé, L.; Schulten, K. *J. Comp. Chem.* **2005**, *26*, 1781–1802.

[56] Stone, J. E.; Phillips, J. C.; Freddolino, P. L.; Hardy, D. J.; Trabuco, L. G.; Schulten, K. *J. Comp. Chem.* **2007**, *28*, 2618–2640.

[57] Chai, J.-D.; Head-Gordon, M. *J. Chem. Phys.* **2008**, *128*, 084106.

[58] Shao, Y. et al. *Phys. Chem. Chem. Phys.* **2006**, *8*, 3172–3191.

[59] Krueger, B. P.; Scholes, G. D.; Fleming, G. R. *J. Phys. Chem. B* **1998**, *102*, 5378–5386.

[60] Madjet, M. E.; Abdurahman, A.; Renger, T. *J. Phys. Chem. B* **2006**, *110*, 17268–17281.

[61] Okiyama, Y.; Watanabe, H.; Fukuzawa, K.; Nakano, T.; Mochizuki, Y.; Ishikawa, T.; Ebina, K.; Tanaka, S. *Chem. Phys. Lett.* **2009**, *467*, 417–423.

[62] Mochizuki, Y.; Koikegami, S.; Amari, S.; Segawa, K.; Kitaura, K.; Nakano, T. *Chem. Phys. Lett.* **2005**, *406*, 283–288.

[63] Nakano, T.; Kaminuma, T.; Sato, T.; Akiyama, Y.; Uebayasi, M.; Kitaura, K. *Chem. Phys. Lett.* **2002**, *351*, 475–480.

[64] Valleau, S.; Eisfeld, A.; Aspuru-Guzik, A. *J. Chem. Phys.* **2012**, *137*, 224103.

[65] Niedzwiedzki, D.; Blankenship, R. *Photosynth. Res.* **2010**, *106*, 227–238.

[66] Saga, Y.; Harada, J.; Hattori, H.; Kaihara, K.; Hirai, Y.; Ohoka, H.; Tamiaki, H. *Photochem. Photobiol. Sci.* **2008**, *7*, 1210–1215.

[67] Furumaki, S.; Yabiku, Y.; Habuchi, S.; Tsukatani, Y.; Bryant, D. A.; Vacha, M. *J. Phys. Chem. Lett.* **2012**, *3*, 3545–3549.

[68] Sarovar, M.; Ishizaki, A.; Fleming, G. R.; Whaley, K. B. *Nat. Phys.* **2010**, *6*, 462–467.

[69] Ganapathy, S.; Oostergetel, G. T.; Reus, M.; Tsukatani, Y.; Gomez Maqueo Chew, A.; Buda, F.; Bryant, D. A.; Holzwarth, A. R.; de Groot, H. J. M. *Biochemistry* **2012**, *51*, 4488–4498.

- [70] Ishizaki, A.; Calhoun, T. R.; Schau-Cohen, G. S.; Fleming, G. R. *Phys. Chem. Chem. Phys.* **2010**, *12*, 7319–7337.
- [71] Zhu, F.; Galli, C.; Hochstrasser, R. M. *J. Chem. Phys.* **1993**, *98*, 1042–1057.
- [72] Bradforth, S. E.; Jimenez, R.; van Mourik, F.; van Grondelle, R.; Fleming, G. R. *J. Phys. Chem.* **1995**, *99*, 16179–16191.
- [73] Yamazaki, I.; Akimoto, S.; Yamazaki, T.; S. Sato, Y. S. *J. Phys. Chem. A* **2002**, *106*, 2122–2128.
- [74] Goodson, T. *Acc. Chem. Res.* **2005**, *38*, 99–107.
- [75] Collini, E.; Scholes, G. D. *J. Phys. Chem. A* **2009**, *113*, 4223–4241.
- [76] Donehue, J. D.; Varnavski, O. P.; Cemborski, R.; Iyoda, M.; Goodson, T. *J. Am. Chem. Soc.* **2011**, *133*, 4819–4828.
- [77] Parkhill, J. A.; Tempel, D. G.; Aspuru-Guzik, A. *J. Chem. Phys.* **2012**, *136*, 104510.
- [78] Zare, R. *Angular Momentum*; Wiley-Interscience: New York, 1988.

TABLE I: Results from MD/TDDFT calculations. Averages and standard deviations of the site energies, relaxation times of the site energies, the pure dephasing rates, and reorganization energies are provided for *syn* and *anti* monomers.

	$\langle \epsilon \rangle (\text{cm}^{-1})$	$\sqrt{\langle \epsilon^2 \rangle} (\text{cm}^{-1})$	$\tau (\text{fs})$	$\gamma (\text{cm}^{-1})$	$E_R (\text{cm}^{-1})$
<i>syn</i>	15243.0	532.2	8.88	938.8	658.7 (266.5) ^a
<i>anti</i>	15319.4	556.5	4.51	525.8	719.9 (298.5) ^a

^aReorganization energies calculated from the spectral densities with the standard prefactor. [33]

TABLE II: Energy transfer time scales obtained from our simulations in comparison with the experimental time scales.

Theoretical time scales	
Decoherence time	40-50 fs
Equilibration over single roll	8.1-14.1 ps
Inter-layer transfer	1.1-1.4 ps
Inter-roll transfer	69.8 ps
Fluorescence anisotropy decay	30 fs
Experimental time scales	
One-color TA anisotropy decay (720-790 nm) [16]	1.7-3.9 ps
One-color TA (720-790 nm) [17]	200-300 fs, 1.7-1.8 ps, 5.4-5.9 ps, 30-40 ps
Two-pulse photon echo (740-780 nm) [18]	140 fs, 1 ps, 10 ps, 280 ps
Two-color TA (685 nm pump, 758 nm probe) [22]	120 fs, 1.1-1.2 ps, 12-14 ps, 46-52 ps
2-D spectral line-shape dynamics [23]	40 fs ^a

^a Decay time of the amplitude at the position of initial maximum [23].